

# Design and Implementation of a Transmit/Receive Ultrasound Phased Array for Brain Applications

Hao-Li Liu<sup>1</sup>, Member, IEEE, Chih-Hung Tsai, Chen-Kai Jan, Hsin-Yu Chang, Sheng-Min Huang,

Meng-Lin Li, Member, IEEE, Weibao Qiu<sup>2</sup>, Senior Member, IEEE,

and Hairong Zheng<sup>3</sup>, Senior Member, IEEE

**Abstract**—Focused ultrasound phased array systems have attracted increased attention for brain therapy applications. However, such systems currently lack a direct and real-time method to intraoperatively monitor ultrasound pressure distribution for securing treatment. This study proposes a dual-mode ultrasound phased array system design to support transmit/receive operations for concurrent ultrasound exposure and backscattered focal beam reconstruction through a spherically focused ultrasound array. A 256-channel ultrasound transmission system was used to transmit focused ultrasonic energy (full 256 channels), with an extended implementation of multiple-channel receiving function (up to 64 channels) using the same 256-channel ultrasound array. A coherent backscatter-received beam formation algorithm was implemented to map the point spread function (PSF) and focal beam distribution under a free-field/transcranial environment setup, with the backscattering generated from a strong scatterer (a point reflector or a microbubble-perfused tube) or a weakly scattered tissue-mimicking graphite phantom. Our results showed that PSF and focal beam can be successfully reconstructed and visualized in free-field conditions and can also be transcranially reconstructed following skull-induced aberration correction. *In vivo* experiments were conducted to demonstrate its capability to preoperatively and semiquantitatively map a focal beam to guide blood–brain barrier opening. The proposed system may have potential for real-time guidance of ultrasound brain intervention, and may facilitate the design of a dual-mode ultrasound phased array for brain therapeutic applications.

**Index Terms**—Blood–brain barrier (BBB) opening, coherent beam formation, dual transmit/receive mode, transcranial brain therapy, ultrasound phased array.

## I. INTRODUCTION

**F**OCUSED ultrasound has been shown to be useful in medical applications for the treatment of conditions related to bone metastasis, uterine fibroid, prostate, and the

central nervous system (CNS) [1]–[6]. In terms of CNS diseases, a tremor treatment that has recently received clinical approval uses an MRI-guided focused ultrasound procedure to transcranially deliver concentric energy deep into CNS tissue to induce a thermal ablative effect [3]. In addition to CNS thermal ablation, administering microbubbles into circulation during focused ultrasound exposure has been shown to temporally induced a blood–brain barrier (BBB) opening effect [7], [8] and to have potential for the delivery of small-molecule anticancer drugs [9]–[11], macromolecular monoclonal antibodies [12], [13], novel theranostic nanoparticles [14], [15], or genes [16], [17] into the CNS, raising the potential of using focused ultrasound as a therapeutic delivery platform across the BBB, which otherwise blocks nearly 98% of drugs [18]. Without administering microbubbles, applying pulsed mode ultrasound into CNS has been shown to effectively perform neuromodulation on rodent [19], [20], primate [21], or human [22], offering another intervention modality using focused ultrasound for brain disease treatment.

Unlike the application of thermal ablation, focused ultrasound (FUS)-induced BBB opening delivers millisecond-level short bursts of energy into CNS tissue. Current MR-guided procedures apply low exposure levels to raise temperatures to harmless levels, and rely on temperature-related proton-resonance-frequency shift to identify focused ultrasound exposure peaks. Some novel studies have used acoustic radiation force imaging (ARFI) to identify the focal beam pattern [23]–[26], but because the focal beam patterns cannot be easily visualized at submegapascal pressure levels, ARFI requires excessively high pressure, typically several megapascals [25], to achieve a sufficiently high contrast-to-noise ratio level to clearly identify the focal beam patterns, yet the pressure for FUS-induced BBB opening was typically at submegapascal level [27]. Currently, FUS-induced BBB opening relies on postoperative confirmation via contrast-enhanced medium leakage, such as gadolinium-diethylenetriamine penta-acetic acid in MRI. Identifying focal beam patterns prior to ultrasound intervention will greatly improve the treatment quality and safety.

One potential approach to realizing real-time intraoperative beam mapping is to integrate diagnostic ultrasound to passively receive backscattered emissions resulting from the therapeutic transducer and to perform reconstruction (or so-called “passive imaging”). In this design scenario, a diagnostic ultrasound probe is often coaxially arranged with the focused

Manuscript received June 5, 2018; accepted July 9, 2018. Date of publication July 12, 2018; date of current version October 3, 2018. This work was supported in part by the Ministry of Science and Technology, Taiwan, under Grant 105-2221-E-182-022 and Grant 106-2221-E-182-02 and in part by Chang Gung Memorial Hospital, Taiwan, under Grant CIRPD2E0051-53 and Grant CMRPD2D0111-13. (Corresponding author: Hao-Li Liu.)

H.-L. Liu, C.-H. Tsai, C.-K. Jan, and H.-Y. Chang are with the Department of Electrical Engineering, Chang Gung University, Taoyuan 333, Taiwan, and also with the Department of Neurosurgery, Chang Gung Memorial Hospital, Taoyuan 333, Taiwan (e-mail: haoliliu@mail.cgu.edu.tw).

S.-M. Huang and M.-L. Li are with the Department of Electrical Engineering, National Tsing Hua University, Hsinchu 300, Taiwan (e-mail: mlli@ee.nthu.edu.tw).

W. Qiu and H. Zheng are with the Paul C. Lauterbur Research Center for Biomedical Imaging, Institute of Biomedical and Health Engineering, Shenzhen Institutes of Advanced Technology, Chinese Academy of Sciences, Shenzhen 518055, China.

Digital Object Identifier 10.1109/TUFFC.2018.2855181

0885-3010 © 2018 IEEE. Personal use is permitted, but republication/redistribution requires IEEE permission.

See [http://www.ieee.org/publications\\_standards/publications/rights/index.html](http://www.ieee.org/publications_standards/publications/rights/index.html) for more information.

ultrasound transducer to collect multiple-channel backscattered acoustic RF data. The emission energy distribution is then reconstructed via the frequency [28]–[30] or time domain [27], [31]–[35] based on passive beam formation theory originally developed for seismic source identification [36], [37]. Passive imaging has recently attracted considerable interest in ultrasound research due to its potential to map bubble activity during cavitation-enhanced therapy, thereby enhancing the treatment safety and outcome assessments [27], [32]–[35]. Microbubbles can be used to detect ultrasound patterns down to 0.5 MPa with a 2-min exposure time [27]. It has also previously been shown, given good synchronization between therapeutic exposure/diagnostic backscattered reception, focal beam reconstruction can be performed at the submegapascal level without microbubbles [38], [39]. However, current diagnostic ultrasound with the frequency ranging 2–10 MHz results in severe transcranial energy loss and aberration and is ineffective for beam pattern reconstruction for CNS application.

Aside from the separate transmission/receiving transducer design, another alternative is to match the backscatter reception to the transmission ultrasound frequency range to improve transcranial detectability. O'Reilly *et al.* [40] designed a lateral-mode vibration large-scale hemispherical phased array structure, with a polyvinylidene difluoride (PVDF) membrane sparsely distributed over the hemisphere to locate the microbubble activation source. Their results suggest that the microbubble distribution can be monitored in high resolution, raising potential for real-time monitoring of the BBB-opening process. Haritonova *et al.* [31] recently used a dual-mode hemispherical 1-D array to transmit therapeutic energy and receive backscattered energy with an identical array element. They demonstrated that the piezoelectric element has the potential to transmit therapeutic energy while also receiving a backscattered signal and showed the feasibility of performing passive beamforming and visualizing the focal beam prior to focused ultrasound treatment through the same 1-D phased array for thermal therapy guidance.

This study proposes a dual-mode hemispherical phased array system design to support the dual function of therapeutic energy emission/passive beam receiving from the same spherically focused array element. We extend our previous transmission system design [41] that supports multiple-element transmission excitation/receiving and attempt to demonstrate the feasibility of passive beamformation imaging to visualize the focal beam pattern, with the aim of monitoring focal beam distribution and providing brain therapy guidance.

## II. THEORETICAL DERIVATION OF COHERENT BEAM FORMATION VIA A SPHERICALLY FOCUSED ARRAY

Focused ultrasound emissions produce spatial wave interference and backscattered acoustic waves when waves encounter scatterers. Since backscattered waves theoretically propagate spherically from the scatterer, the origin of the backscattered signals can be used to determine the scatterer location by calculating the arrival time at a piezoelectric element. To accurately reconstruct the backscattered acoustic wave from

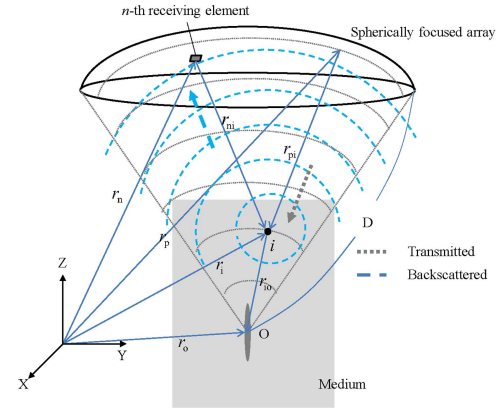


Fig. 1. Geometric relationship showing the concept of the coherent backscattered emission beamformation implemented for the 2-D spherically focused ultrasound array.

a designated scatterer point, a fixed source location ideally gives the same difference in the arrival time for a set of receivers and, inversely, changes in arrival times can be used to identify different source locations. This approach requires identifying the source position of the backscattered acoustic wave based on the acoustic wave signal received from multiple elements under a transmission/receiving sequence synchronization to detect the transmitted patterns under low-pressure short-cycle burst exposure conditions. A given source location always gives a predetermined time-of-arrival. Under perfect transmit/receive synchronization conditions, it is feasible to designate exact time of arrival for the backscattered acoustic waves originating from specific target positions.

Fig. 1 shows how the position information is localized and reconstructed at a selected target point that is ultrasonically excited by multiple piezoelectric ultrasonic elements. Assume the  $n$ th element is one among a total  $N$  receiving channels located on the concave and spherically focused array, and coherently receives the backscattered acoustic ultrasound RF emission originating from the spatial position  $r_i$ , denoted by  $s_n(\vec{r}_i, t_n)$ . The proposed approach considers all backscattered emissions, and then coherently sums the contribution of each acoustic emission received by the array, with a time delay  $t_n$ . Here,  $\vec{r}_i$  is defined as the receiving ray path of a single source point, and  $r_n$  is the spatial position of the  $n$ th element, which can easily derive the relative distance as  $\vec{r}_{ni} = |\vec{r}_n - \vec{r}_i|$ . The beamformed signal at the  $r_i$  position can be obtained as

$$S(\vec{r}_i) = \sum_{n=1}^N A_{ni} \times s_n(\vec{r}_{ni}, t_i) \quad (1)$$

where  $A_{ni}$  is the weighting factor for each receiving element,  $s_n(\vec{r}_{ni}, t_n)$  represents the received backscattered RF data on the  $n$ th receiving element on the spherically focused array,  $t_i$  is the total delay contributed by the delay including the wave transmission phase and the receiving phase, and  $t_i = t_t + t_r$ . Here,  $t_t$  is the transmission traveling time of the spherically concave wave propagation simultaneously emitted from the

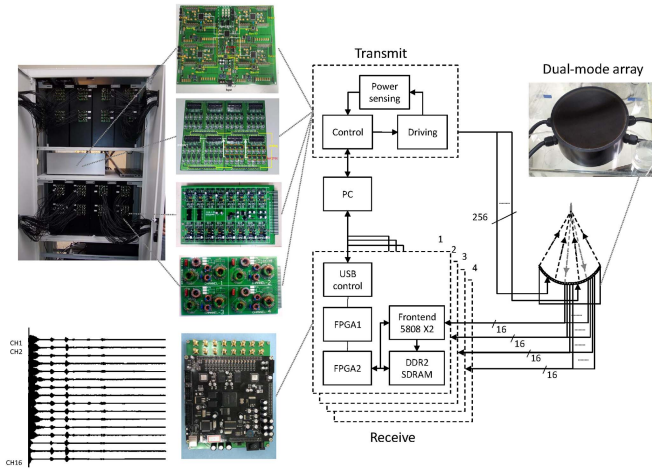


Fig. 2. Block diagram of the dual transmission/receiving focused ultrasound system. The four 16-channel receiving modules were integrated with the transmission system to perform the dual transmission/receiving function through a 256-channel spherically curved ultrasound phased array transducer.

array elements and can be calculated as

$$t_t = \frac{\overline{r_{pi}}}{c} \quad (2)$$

where  $\overline{r_{pi}}$  is the distance the wave travels from the concave transducer plane to  $\vec{r_i}$ , and  $c$  is the speed of sound. The distance  $r_{pi}$  can be easily calculated as  $\overline{r_{pi}} = D - \overline{r_{io}}$ , where  $D$  is the curvature radius of the concave array, and  $r_{io}$  is the Euclidian distance between  $i$  and the geometrical focal position. In addition, the time delay caused by backscattering can be rewritten as

$$t_r = \frac{\overline{r_{ni}}}{c}. \quad (3)$$

Equation (1), which correlates to the pressure level located at  $\vec{r_i}$ , can be derived as

$$S(\vec{r_i}) = \sum_{n=1}^N A_{ni} \times s_n \left( \overline{r_{ni}}, \frac{\overline{r_{pi}}}{c} + \frac{\overline{r_{ni}}}{c} \right). \quad (4)$$

### III. MATERIALS AND METHODS

#### A. Multiple-Channel RF Driving System Design

We previously developed a 256-channel phased array driving system to transcranially induce BBB-opening [41], which is used to drive multiple-channel transmission in the present study (see Fig. 2). The multiple-channel transmit system comprises two major circuit modules: a central transistor-transistor logic (TTL) control kernel and the 256-channel power-feedback RF driver described as follows. In the central TTL control kernel, we modified our previous design by using a cascade-microcontroller/field-programmable-gate-array (micro-controller unit (MCU)/FPGA)-based embedded system structure that generates 256-channel phasing TTL signal outputs. Via a simple latch circuit design in the FPGA, the excitation period can be precisely controlled from a single-cycle output to a continuous-wave output. The system's

operation frequency is tunable, and can simultaneously generate outputs from multiple operating frequencies.

The programed FPGA produced TTL phasing signals to support an operating frequency range from 200 kHz to 1.2 MHz (500 kHz in this study) and provides 8-bit phase resolution for the transmission pulse (i.e., a phase resolution of  $1.4^\circ$  per channel). The driving circuit used a self-designed MCU-controlled dc power supply. The output dc voltage was supplied from a self-designed MCU-controlled dc-to-dc buck converter, which could be controlled by pulsewidth-modulation (PWM) signals from the MCU. The output voltage was adjustable through the control panel. The maximum power output was designed to be 10 W for each channel, with a maximum total electrical power output of 1000 W. The system's output power could be regulated by the PWM-controlled buck dc supply, as well as the control kernel, providing flexibility to generate TTL outputs with various duty cycles. The RF amplifier was designed so that the 256-channel TTL phasing signal could be fed into differential amplifier modules to allow for current driving. A half-bridge dc-to-ac inverter constructed using high-voltage MOSFETs was used to generate a high-voltage output, and high-voltage diodes were used to deal with high-voltage switching transients.

#### B. Multiple-Channel Receiving Module Design

To implement the dual-mode function on the spherically focused ultrasound array, a multiple-channel receiving module was designed and implemented in the system (see Fig. 2). The RF receiving circuit adopted a modular design, with each module receiving 16 channels, and modules can be cascaded in parallel to extend to receiving  $16 \times M$  channels, where  $M$  represents the total number of receiving modules. Each receiving module features cascaded a two-stage FPGA architecture, where the first-stage FPGA (Stratix, Altera, San Jose, CA, USA) connects the universal serial bus (USB) controlled MCU (CyUSB3014, Cypress Semiconductor, CA, USA; data transmission up to 300 MB/s) and receiving synchronous trigger signals fed from the 256-channel transmission system. The second-stage FPGA (Stratix, Altera) connected to two 8-channel ultrasound receiving front-end ICs (5808A, TI; operating with a sampling frequency of 40 MHz and 14-bit resolution) and a T/R switch circuit to achieve 16-channel backscattered signal reception. With the controlled parameters set in the internal static random-access memory (SRAM), the second-stage FPGA also externally connects to double-data rate 2 synchronous dynamic random-access memory to temporally restore the data of each RF channel through a first-in first-out data transmission protocol. A single 16-channel reception module allows for fast data collection (50  $\mu$ s/channel receiving), and temporal RF data storage with individual RF signal storage of up to 32 kB (allowing 200- $\mu$ s RF data storage under the 40-MHz sampling frequency). The module can perform on-board delay-and-sum operations under a designated delay table assigned in the SRAM of the second-stage FPGA or can retrieve single-channel RF data for offline postprocessing analysis. (This study used channel data retrieval, with beam formation processed off line).



To extend the reception channel beyond 16 channels, multiple 16-channel receiving modules were serially linked to share an identical single TTL trigger signal from the central control kernel or the 256-channel transmission system for intermodule synchronization as well as RF data synchronization. In this study, four 16-channel receiving modules were cascaded for a total of 64 reception channels.

### C. Spherically Focused Ultrasound Phased Array

This study used a spherically curved ultrasound phased array. The concave array consists of 256 channels made of piezocomposite material, and designed with a high focal geometry (diameter = 120 mm, curvature radius = 100 mm, F-number = 0.83, active part diced into  $5.5 \times 5.5$  mm elements, Imasonic Inc., Besancon, France). The center frequency of this array is 500 kHz, but it provides bandwidth that allows operation between 400 and 600 kHz. To electrically match the concave array element to connect to the 256-channel transmit system, a transformer-type impedance transformation configuration is used to provide wideband power transmission. To test the dual-mode capability, up to 64 out of the 256 elements were selected to shunt the connection to the receiving module channels via a T-type Bayonet Neill–Concelman connector.

### D. Data Processing

Beam formation of the backscattered emission retrieved from the spherically focused array was postprocessed using MATLAB (Mathworks, Natic, MA, USA). First, the multiple-channel RF receiving data was filtered with a second-order bandpass filter (center frequency set to 500 kHz, 40% bandwidth). In the selected analyzed imaging frame, RF beam formation was conducted for each grid point based on the beam formation method described earlier. (To simplify the investigation, the apodization weighting factor was set to unity to give equal consideration to the gain compensation for each channel signal.) After beamforming, the coherent RF beamformed data was then demodulated, and time gain compensation was applied in tissue-mimicking phantom study cases. The processing time for each  $100 \text{ mm} \times 100 \text{ mm}$  imaging (1-mm grid) frame was estimated to be  $\sim 15$  min in an Intel I5 PC environment. To improve the signal-to-noise ratio and focal beam detectability in transcranial experiments, phase aberration correction over the received RF channel signals was performed to restore the focal reconstruction (with the focal point serving as the reference corrected position). To correct aberration of the received backscattered RF signal resulting from the inserted skull cadaver, a previously described phase correction approach was implemented (with uncorrected amplitude) to restore point spread function (PSF) and focal beam formation [40], [42]. The corrected beam formation applied in (4) can then be rewritten as

$$S_{\text{corr}}(\vec{r}_i) = \sum_{n=1}^N A_{ni} \times s_n \left( \frac{\vec{r}_{pi}}{c} + \frac{\vec{r}_{ni}}{c} - \frac{\Delta\theta_n}{\omega_0} \right) \quad (5)$$

where  $\Delta\theta_n$  is the corrected phase applied to the  $n$ th receiving channel and  $\omega_0$  is the transmit angular frequency.  $\Delta\theta_n$  in

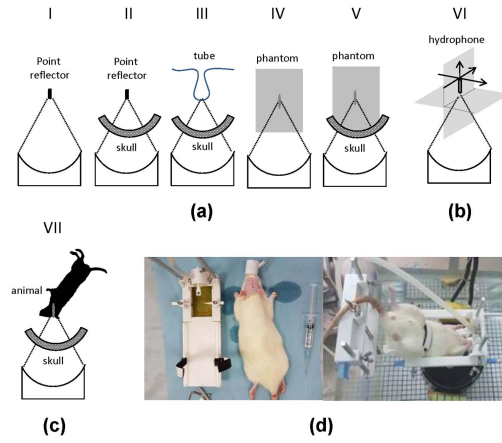


Fig. 3. (a) Experimental setup of the backscattered receiving for PSF/beam deposition formation and reconstruction. (b) Experimental setup for transmission focal beam pressure measurement. (c) and (d) *In vivo* experimental setup with focal beam penetrating through the human cranial bone.

each channel was calculated via channel-to-channel RF data correlation analysis with the reference of free-field RF measurements. The corrected phase performed at the steering position was then applied to correct all spatial sample points. To evaluate the performance of the reconstructed maps, the mainlobe-to-sidelobe ratio (denoted as MSR, presented in decibels) was estimated and is defined as the ratio of the mainlobe magnitude to the standard deviation of the background sidelobe magnitude.

### E. In Vitro Experimental Setup

The *in vitro* experiment evaluates the PSF as well as focal beam distribution mapping via the spherically focused dual-mode ultrasound phased array. For image reconstruction, the transmit pulse is typically set to a burst length of two cycles (0.004 ms), a pulse repetition frequency (PRF) of 2 Hz, and a negative pressure output of 0.3–1.3 MPa. Receiving circuits with channel numbers ranging from 4 to 64 received the RF signals. A total of five-type *in vitro* experiments were conducted [see Fig. 3(a)].

- 1) *Free-field point reflector (Setup I)*: This setup aims to evaluate the free-field PSF generated by the dual-mode spherically focused array. A metallic point reflector (with a ball-shaped tip made of stainless steel with a 1-mm reflector end) was positioned at the geometrical center of the phased array immersed in a degassed-water filled tank with absorbent material attached to the inner wall to reduce reflection. The water tank size was  $300 \text{ mm} \times 300 \text{ mm} \times 300 \text{ mm}$ .
- 2) *Transcranial Point Reflector (Setup II)*: This setup evaluates the transcranial PSF performance of the dual-mode hemispherical array. The experimental setup is identical to (1) but using a human skull (with a distance of  $\sim 30$  mm between skull base and reflector) to measure the PSF transcranially.
- 3) *Transcranial Microbubble Detection (Setup III)*: To evaluate the transcranial PSF generation induced by microbubbles (Sonovue, Bracco Diagnostics Inc., Milan,

Italy; mean size = 2–5  $\mu\text{m}$ ), a tube phantom was set up with flowing microbubbles. Polyethylene tubing (PE-50, Intramedic) was used (OD = 965  $\mu\text{m}$  and ID = 580  $\mu\text{m}$ ) with an average flow rate of approximately 10 mL/min. The PSF induced from microbubble concentrations ranging from 0.01%–1% was tested. During measurement, the PE tube was curved to form a small loop shape to minimize the cross-sectional area and position it at the geometrical center. The formalin-preserved skull was degassed prior to the experiment [42], and during the experiment, the skull was positioned in the tank with the focal beam penetrating through the skull and aiming at the tube.

- 4) *Focal Beam Detectability in Tissue-Mimicking Scattering Phantom (Setup IV)*: A soft-tissue-mimicking graphite phantom was made to test the beam formation algorithm's capability to visualize the focal beam deposition in a scattering medium. The phantom measured 80 mm  $\times$  85 mm  $\times$  120 mm with the gradient previously reported [38], [43] to present a speed of sound of the phantoms of 1541 m/s at 22 °C, with a density of 1040 kg/m<sup>3</sup>, and an attenuation coefficient of 0.45 dB/cm/MHz to mimic soft-tissue backscattering behavior.
- 5) *Transcranial Focal Beam Detection in Tissue-Mimicking Phantom (Setup V)*: This setup tested the feasibility of transcranially identifying focal beam deposition with a human skull cap. In transcranial experiments, the skull was placed in the tank with the geometrical center of the array positioned at the center of the graphite phantom. Previous experiments found a transcranial loss of 68%  $\pm$  5% in a testing cadaver at 500 kHz [41].

#### F. Pressure Measurement and Calibration

The free-field pressure field was measured to serve as a comparison to the reconstructed pattern deposition [setup VI, see Fig. 3(b)]. A PVDF needle-type hydrophone (HNP-0400, ONDA, Sunnyvale, CA, USA; calibration range from 50 kHz to 20 MHz) was mounted on a 3-D positioning system to measure the pressure distribution induced by the spherically curved ultrasound phased arrays. The step size was 0.5 mm in the cross-sectional plane (denoted by the  $xy$  plane) and the axial plane (denoted by  $yz$  plane), both with maximum measured distances of  $\pm 30$  mm.

#### G. In Vivo Experimental Design

All animal procedures were approved by the Institutional Animal Care and Use Committee of Chang Gung University and adhered to the experimental animal care guidelines. A total of eight adult male rats (250–300 g) were exposed to focused ultrasound emission to induce BBB opening. MRI scans of the rat brains were performed one day prior to *in vivo* animal experiments to serve as a high-resolution anatomical reference for backscattered ultrasound reconstructed maps. T2-weighted images were acquired from an animal-purposed seven-T MRI (ClinScan, Bruker, Germany; pulse repetition time (TR)/echo time (TE) = 1600/41 ms, FOV = 28  $\times$  41 mm<sup>2</sup>, in-plane

resolution = 0.16  $\times$  0.16 mm<sup>2</sup>, slice thickness = 0.6 mm, and flip angle = 180°). Markers were attached to the animals' shaved scalps throughout experimental process to align MRI and backscattered focal beam reconstruction with the procedure previously described [38].

Prior to FUS exposure, the animal's scalp was first shaved with clippers and a PE-50 catheter was inserted into the tail vein. The animals were anesthetized with 2% isoflurane, and then laid supine on the self-designed animal holder (the bottom of which contains a thin-film sealed window to allow focal beam penetration) with the animal head positioned to allow the focal beam to aim at the targeted brain hemisphere [denoted by setup VII, see Fig. 3(c)]. To induce BBB opening, the system was switched to long-burst excitation mode, with a 1-ms burst FUS exposure delivered (PRF = 10 Hz, exposure time = 120 s, and transcranial pressure = 0.15/0.53 MPa). SonoVue SF6-coated ultrasound microbubbles (2–5  $\mu\text{m}$ , 0.3 mL/kg; Bracco Diagnostics Inc., Milan, Italy) were administered intravenously. Before and after microbubble administration, the driving system switched to short burst mode to generate a 20-cycle burst for channel RF backscattered emission reception, and image reconstruction was processed offline. Signal intensities at the target area were measured and compared between the two reconstruction maps.

Fig. 3(d) shows the animal positioning arrangement to fit the 256-channel dual transmission/receiving mode ultrasound phased array system during the *in vivo* BBB-opening experiments. The holder allowed the geometrical focal beam position to align with the target hemisphere of the animal brain. The human cranial bone was inserted between the spherically focused phased array and the animal fixation holder. Prior to microbubble administration, the system performed a short 20-cycle transmit/receive sequence to obtain the 32-channel backscattered emissions, and long-burst exposure to induce BBB opening (1-ms burst length, PRF = 10 Hz, and exposure time = 120 s). The exposure levels of the preoperationally 20-cycle short burst and intraoperatively 1-ms long burst were set identically in each experiment (0.15/0.53 MPa to induce various degrees of BBB opening). We then evaluated the correlation of the mapping magnitude with the BBB-opening scale based on the penetrated concentration of Evans blue (EB)-albumin complex (molecular weight = 67 kDa). All image reconstructions were subjected to skull-induced aberration correction to compensate for phase aberrations introduced by the inserted human cranial bone. The EB-albumin complex quantification procedure is described previously in [41].

## IV. RESULTS

We first tested the capability of PSF reconstruction via a strong scattering point reflector. Fig. 4(a) compares the reconstructed PSF with varying receiving channels (with element numbers ranging from 4 to 64) to characterize beamformation performance and its dependence on the number of receiving channels. Fig. 4(b) shows the PSFs theoretically established from the full channel (256) for comparison (simulated under K-wave/MATLAB environment). Four to eight receiving channels did not provide sufficiently high PSF discrimination from

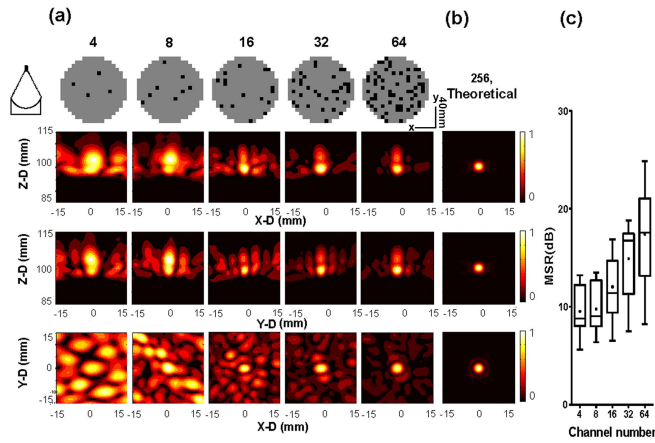


Fig. 4. (a) and (b) Measured and beamformed PSFs using 4–64 randomly distributed receiving channels (receiving channel positions marked in black) via the 256-element spherically focused array for a two-cycle burst. The PSF formation was measured under a point reflector setup (setup I). All subplots in (a) and (b) are self-normalized. (c) MSR analysis under various receiving channel conditions. Averaged MSR levels were marked as “+.”

the surrounding sidelobes and exhibited unsatisfactorily low MSR levels ( $<10$  dB, respectively). Increasing the number of receiving channels to 16 improved MSR to 12.5 dB, while the MSR level at 64 channels has the highest MSR level of 18.5 dB among the testing conditions. The measured PSF contains a larger dimension along the axial direction than the radial one ( $-3$ -dB dimension = 4.5 and 3.9 mm, respectively, at the 16-channel receiving case), and taillike grating lobes were seen behind the focal depth, mainly caused by imperfections in the point scatterer. Moreover, the measurements showed apparent sidelobes (particularly, on the cross-sectional plane) which induced a relatively low MSR level. As the receiving channel increased, the reconstructed PSF showed a tendency to approximate the ideal PSF distribution [Fig. 4(b), theoretical MSR = 72 dB].

The impact of the receiving channel distribution was then investigated (with the number of receiving channels fixed at 16). Aligning the receiving element to be distributed in 1-D only provides high PSF performance in one axial plane, but failed to provide spatial resolution in another [Fig. 5(a)]. The asymmetry of the PSF can also be clearly observed from the cross-sectional plane. Centrally allocating the receiving element induces a larger in-plane PSF dimension (12 mm) as well as a poor spatial resolution along the cross-sectional plane; due to the equivalently reduced aperture size [Fig. 5(b)], PSF dimension along the axial direction was unaltered due to the transmit pulse cycle being unchanged. When the receiving elements are regularly distributed [Fig. 5(c)], a regular grating lobe pattern is observed in the PSF map, whereas in Fig. 5(d), the grating lobes tended to be irregularly distributed. This suggests that the wide distribution of receiving elements can improve PSF resolution due to the extended aperture size.

We then investigated the influence of the transmit pulse cycle on PSF. In this comparison and the following investigation, the number of receiving channels was set at 32. Fig. 6 shows the influence of different pulse lengths on

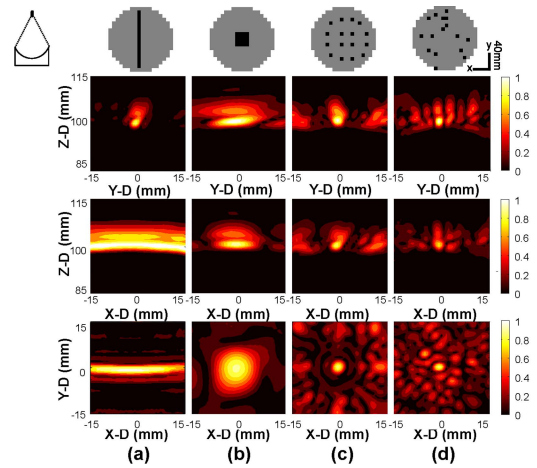


Fig. 5. Reconstructed PSFs under different receiving channel arrangements in the 256-element spherically focused array (receiving channels = 16 for every case, with the position marked in black, burst cycle = 2, and all subplots are self-normalized). (a) 1-D linear arrangement. (b) Central distribution. (c) Regular distribution. (d) Random distribution. The PSF formation was measured under a point reflector setup (setup I).

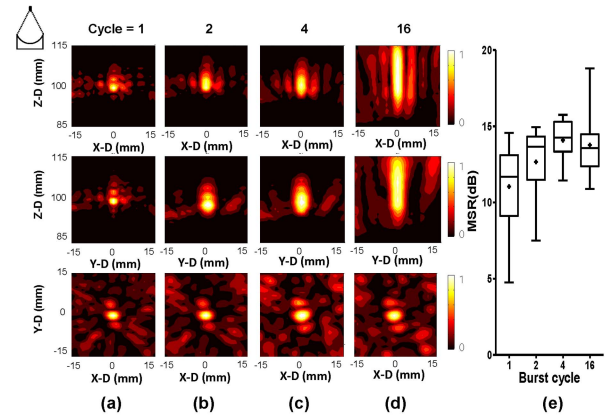


Fig. 6. (a)–(d) Reconstructed PSFs under different transmission pulse lengths (transmission cycles = 1, 2, 4, and 16, with the receiving channels fixed at 32, all subplots are self-normalized). The PSF formation was measured under a point reflector setup (setup I). (e) MSR analysis of the condition. Average marks as “+.”

PSF [from 1 to 16 cycles, Fig. 6(a)–(d)] with the corresponding MSR analysis [Fig. 6(e)]. Single-cycle transmission reconstructed PSF with the highest axial resolution; however, increasing transmission cycle improved in-plane MSR due to the suppression of sidelobes [see Fig. 6(e), the MSR can be improved from 10.8 to 13.9 dB as the transmission cycle increased from 1 to 4]. For transmission cycle set to 16, the PSF dimension profoundly increased yet with the MSR level fell (13.7 dB). Setting a burst cycle of 2 maintained sufficiently high MSR and spatial resolution, and was considered to be a proper solution for PSF reconstruction.

We then evaluate PSF reconstruction under the experimental setup using a point reflector or microbubble-perfused PE tube as a strong reflector to penetrate through human skull. The human cranial bone was positioned between the reflector and the spherically focused phased array. The transmission cycle was set to 2, and the backscattered emissions were



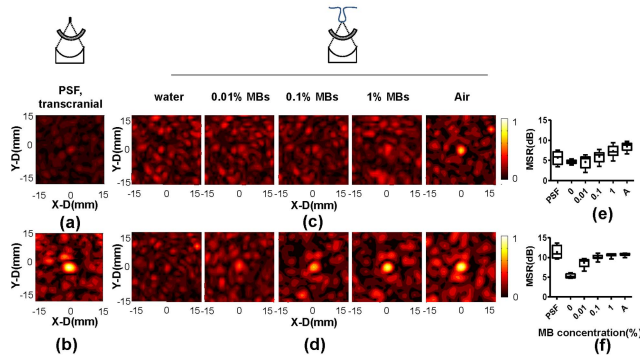


Fig. 7. (a) Transcranially reconstructed PSF using the point reflector as the scatterer (setup II). (b) Reconstructed PSF in (a) but with an additional phase aberration correction. (c) Transcranially reconstructed PSFs when using a microbubble presented PE tube as the scatterer, with various microbubble concentrations (setup III). (d) Reconstructed PSFs in (b) but with an additional phase aberration correction. Transmission cycle fixed = 2 and receiving channels = 32. All subplots from (a) to (d) were normalized to the peak main lobe level of Fig. 9(b). (e) MSR analysis for the condition of (c). (f) MSR analysis for the condition of (d). Averaged MSR levels were marked as “+.”

transcranially collected via 32 receiving channels. Fig. 7(a) shows the transcranial reconstructed PSFs from a point reflector, showing that PSF reconstruction failed to obtain sufficiently high MSR due to strong aberrations caused by the skull (setup II). Similarly, without phase aberration correction, it was found that PSF cannot be well reconstructed when various concentrations of microbubbles were perfused into the PE tube, except under conditions of pure-air injection or a sufficiently high microbubble concentration up to 1% [setup III, see Fig. 7(b)]. Phase aberration correction (via the RF signal correlation calculation without applying amplitude correction) and contrast-enhanced processing (via difference estimation between pre- and post-MB injection) were conducted to improve PSF detection sensitivity [40], [42]. Phase aberration correction successfully corrected the phase aberration, and the PSF can be successfully restored [Fig. 7(c)]. Sidelobes cannot be effectively reduced even performing phase correction when compared to free-field PSF reconstruction [compared to setup I in Fig. 6(b) because the correction is only performed to correct phase aberration at the geometrical center, while other field positions were left uncorrected. Phase aberration correction can successfully restore the PSF for microbubble concentrations of at least 0.1% (equivalents to  $10^5$  MBs/mL). Fig. 7(e) and (f) compares the corresponding MSR values revealing significant MSR improvement can be achieved following the phase aberration correction to allow for main lobe identification in transcranial conditions (MSR increase ranging from 5.9 to 9.5 dB), particularly for low MB concentration cases.

The above findings demonstrate that the proposed algorithm can successfully reconstruct PSF using a strong scatterer. The following evaluates the feasibility of using the dual transmit/receive system to reconstruct the focal position map in soft tissue (using a tissue-mimicking graphite phantom as a substitute). Electrically steered focal energy (+4 to −8 mm in-plane steering shift off the geometrical center) was delivered (transmit cycle set to two cycles) from the 256-channel phased

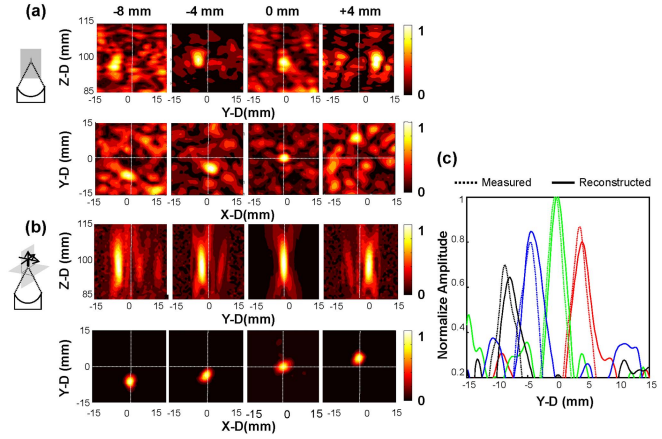


Fig. 8. (a) Reconstructed focal position maps along the cross section at focal depth (100 mm) as well as the axial plane across the steered focus, when steering the focal beam in different locations (+4, 0, −4, and −8 mm off the geometrical center). The emission cycle was set to 2, with the receiving channel set to 32. The maps were presented as in-plane intensity without maximum intensity projection, with all subplots self-normalized. (b) Corresponding hydrophone measured pressure maps with the same plane shown in (a). (c) Profile comparison between the reconstructed (setup IV: solid line) and hydrophone measured (setup VI: dashed line) profiles along the radial (Y-D) directions at  $z = 100$  mm.

array via individual-element phase designation to the tissue-mimicking phantom, with 32 randomly distributed channels to receive the backscattered emission. Fig. 8(a) shows the reconstructed focal position map with the designated focus steering at +4, 0, −4, and −8 mm off the geometrical center. Speckles are clearly observed in the reconstructed maps generated from the scatterers of the inserted tissue-mimicking graphite phantom. However, constructive interference at the designated focused position can still be clearly identified at the steered position when compared with the hydrophone measured pressure profiles [Fig. 8(b)], showing the successful mapping of the steered focal energy position can be achieved in the tissue-mimicking phantom.

Further comparing the restricted focal position maps along the radial direction [see Fig. 8(c)] shows the generally good estimation including main lobe position and magnitude but, as previously described, the discrepancy of the main lobe position gradually increased with the designated increased steering distance. The cross section −3-dB dimension in the reconstructed maps was 3.2 mm, which is close to the measured dimension of 2.7 mm (measured when center steered). Overall, the mapping showed successful reconstruction of the focal beam to identify the steering position in the tissue-mimicking phantom.

Following the successful focal mapping in the tissue-mimicking phantom, we further investigated whether an additional phase aberration correction could be used to map the focus in the graphite phantom under a transcranial setup (Setup V). The steering position was set at the center of the graphite phantom, with 32 receiving channels. To test the focus detectability of the reconstruction with the effect of transmit cycle, the transmit pulseshift varied from 2 to 50 cycles (equivalent to pulse lengths of 4–100  $\mu$ s), with phase aberration correction performed for all reconstructions. The focal

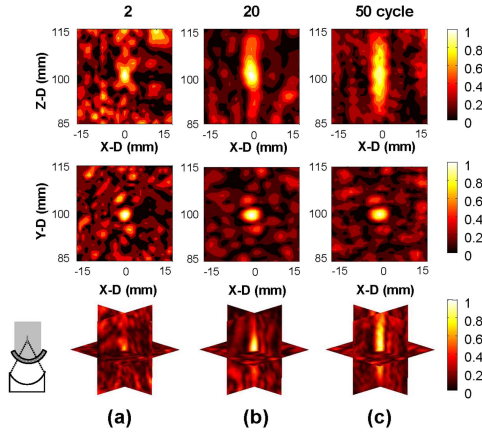


Fig. 9. Reconstructed focal position when transcranially transmit FUS energy in the tissue-mimicking graphite phantom (setup V). (a) Transmission cycle = 2. (b) Transmission cycle = 20. (c) Transmission cycle = 50. Receiving channel number was set to 32. Phase aberration corrections were applied for all focal beam reconstructions. All subplots are self-normalized.

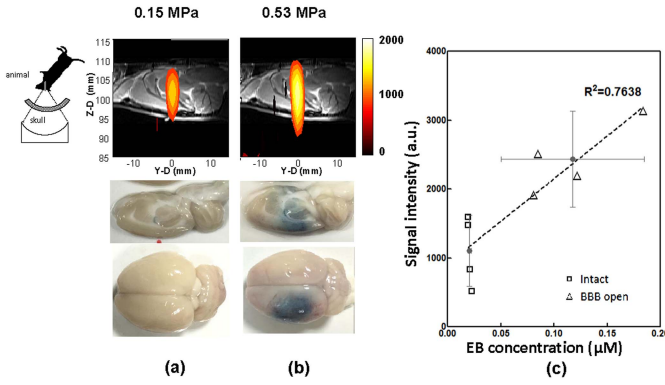


Fig. 10. (a) and (b) Reconstructed focal beam distributions (infused with T2 weighted MRI) to intraoperatively guide the *in vivo* BBB opening procedure for respective exposure levels of 0.15 and 0.53 MPa. The EB-stained brain sections of the same animals are presented. (c) Correlation between the quantitated EB dye leakage and the transcranial beam magnitude. Emission burst cycle = 20 and receiving channels = 32 (setup VII).

beam was found to be capable of being reconstructed in two-cycle transmission conditions [Fig. 9(a)] but with relatively low MSR level (10.5 dB) high sidelobe magnitudes. Increasing the transmission cycle improved focal beam detectability and reduced the sidelobes magnitude [Fig. 9(b) and (c)], compared to main lobe magnitude, due to the suppression of the sidelobes and MSR increase (13.3 and 15.7 dB, respectively). However, the improved MSR was also accompanied by a loss of spatial resolution along the axial direction. The dimension under the 50-/20-cycle transmits condition extended the focus axially to 18.5/6.2 mm, or, respectively, 9 and 3 times greater than that two-cycle transmit condition (2.8 mm). Concurrently, considering the axial resolution and the MSR, the 20-cycle burst was selected for the focal map reconstruction in the following *in vivo* experimental reconstruction.

With the successful transcranial reconstruction of the focal position in the tissue-mimicking phantom, we attempted to guide the focal beam for *in vivo* BBB opening, inserting the human cranial bone between the animal and the array. Fig. 10(a) and (b) compares the reconstructed maps (with

a  $-3$ -dB cutoff to reject sidelobe noise) prior to the long-burst BBB-opening exposure at 0.15 and 0.53 MPa (after considering human skull transcranial loss), as well as comparing the corresponding EB-stained brain sections following animal sacrifice. The 0.15-MPa exposure failed to open the BBB (confirmed by the absence of EB-albumin complex in the brain section). In contrast, the 0.53-MPa exposure successfully induced BBB opening (confirmed by EB-albumin staining at the FUS exposure region). The EB-stained location was colocalized with the MRI-registered reconstructed focal beam locations, validating the use of passively reconstructed maps to assist focal beam guidance. Fig. 10(c) shows the correlations between the quantitated EB concentrations (as an index to represent the BBB-opening scale) to the signal intensity of the reconstructed map ( $n = 8$ ). The 0.15-MPa exposure contributed a signal intensity of  $1106.5 \pm 514.7$  a.u., corresponding to a lower EB concentration of  $0.021 \pm 0.0015$   $\mu\text{M}$ . On the other hand, the 0.53-MPa exposure contributed a significantly higher signal intensity of  $2433.8 \pm 697.1$  a.u., corresponding to a higher EB concentration of  $0.117 \pm 0.067$   $\mu\text{M}$ , reaching a high overall correlation of  $r^2 = 0.7638$ . The *in vivo* experimental results support the feasibility of using preoperatively backscattered-reconstructed focal mapping to gauge the exposure level and guide transcranial FUS treatment.

## V. DISCUSSION

### A. Significance of This Study

This study presents a dual-transmit/receive mode ultrasound phased array system to support concurrent therapeutic energy exposure and reconstruction of the focal energy deposition via received backscattered signals from a dual-transmission/receiving spherically focused array. The experimental results successfully demonstrate the concept feasibility via sparsely arranged element reception, showing that the reconstructed PSF can be successfully built with a spatial resolution close to that theoretically predicted. Second, we showed that the focal distribution can be transcranially reconstructed in a tissue-mimicking phantom with sufficiently high detectability through the application of an additional phase aberration correction procedure. Third, the *in vivo* experimental results show that the proposed dual-mode system design can successfully guide focused ultrasound intervention. The proposed configuration raises the potential for real-time guidance for focused ultrasound therapy, particularly, for applications such as transcranial ultrasound-induced BBB opening or transcranial ultrasound neuromodulation.

### B. Comparison of Noncoherent Passive Cavitation Mapping and Coherent Backscattered Reconstruction

Passive cavitation imaging (PCI) and passive acoustic mapping are based on applying passive cavitation detection with a single-element transducer to multiple-channel emission reception through a 1-D diagnostic ultrasound array. PCI can passively detect emissions generated from (stable or inertial) cavitation activity, but is primarily used to detect violent bubble activity or boiling during high-intensity focused ultrasound thermal ablation [27], [44]. Recently, therapeutic ultrasound



applications with microbubbles have attracted increased attention for use in enhancing drug delivery, capillary permeation, or sonothrombolysis. Therefore, PCI has been used to map microbubble-related cavitation activity without the need for strong ultrasound exposure level [40], [45]–[47]. However, to provide sufficiently high cavitation detectability and sensitivity, time exposure acoustics theory for PCI typically performs mapping in a noncoherent manner via repetitive ray tracing-based emission [36], [37]. The proposed dual transmission/receiving mode phased array relies on backscattered emission reconstruction in a coherent beamformation fashion, which is identical to the traditional beam formation approach, but is implemented in a 2-D spherically focused array. Previously, in a separate transmit/receive transducer arrangement, we demonstrated the coherent-based backscattered focal reconstruction concept can be used to map the focus to guide focused ultrasound BBB opening [38]. One major advantage of coherent beam formation is its high spatial resolution because the reconstructed PSF can reach the theoretical resolution of the order of the wavelength. In addition, unlike the approaches that rely on repetitive exposure calculations and noncoherent summing of the contribution from microbubble-based emissions in PCI, the proposed approach relies on the coherent reconstruction of backscattered emissions from the focal position, providing sufficiently sensitive maps to reconstruct the focus without the need for strong scattering. It also potentially allows for the use of short-cycle transmission without the need of microbubbles for focal position mapping (in comparison, Arvanitis and McDannold [47] used 40–50-cycle emissions with microbubbles during millisecond-level FUS exposures, while O'Reilly *et al.* [40], [48] used 5–50-cycle emissions at 1–100-Hz PRF with microbubbles for passive mapping analysis).

Burgess *et al.* [49] recently proposed the use of synchronized diagnostic ultrasound (18 MHz) with a focused ultrasound device to implement coherent and absolute time-delay passive mapping of microbubble suspension, and confirmed that this configuration significantly improved image quality in mapping cavitation (image PSF can be improved from 2 to 0.15 mm). The PSF resolution (18 MHz and 0.15 mm), compared with the proposed PSF dimension in our proposed system (0.5 MHz and 4.5 mm), was found to have comparable resolution to that used in this study when the imaging frequency was proportionally scaled.

### C. Comparison of the Dual-Mode Approach to the Separated Transducer Approach

PCI is traditionally implemented using separate transmission and reception transducers, typically using a diagnostic 1-D array to record microbubble-related emission events recording with a wideband diagnostic ultrasound operating frequency of 3–8 MHz, while therapeutic ultrasound emission contains a more narrowband frequency in the range of several hundreds of kilohertz. Hence, one key advantage to the separate transducer configuration is wide bandwidth that allows for the reception of wideband emissions for cavitation activity capture and characterization during focused ultrasound therapy. Inertial cavitation has been identified as being

accompanied by violent bubble collapse, tissue vaporization of hemorrhage during exposure [50]–[52], and highly correlates with wideband emission. In addition, a growing number of commercially available diagnostic ultrasound systems support full acquisition of RF channel data, increasing the feasibility of system integration. However, integrating currently available diagnostic ultrasound systems into the therapy array may raise obstacles to stable cavitation detection through a diagnostic ultrasound array because low-frequency emissions such as subharmonics and lower band ultraharmonics are out of the diagnostic ultrasound probe's frequency range. In addition, diagnostic ultrasound has poor skull penetration, and the equivalent therapeutic ultrasound aperture will be substantially reduced, thus degrading therapeutic ultrasound emission efficiency and focusing.

O'Reilly *et al.* [40] proposed a hemisphere therapeutic array that sparsely distributes receiving elements for microbubble activity tracking and mapping, selecting a receiving element frequency to match the specific harmonic band, thus increasing the detection sensitivity of stable cavitation. Previously, the concept of dual transmission/receiving mode phased array system theranostic applications was proposed to concurrently emit continuous-wave focused ultrasound energy and perform backscattered reception for ultrasound thermometry analysis [53], [54] with a demonstration to guide focused ultrasound thermal therapy in small animal brains [31]. In this study, we attempt to demonstrate a dual-transmission/receiving configuration at a frequency suitable for transcranial applications penetrating the human skull (i.e., 500 kHz), and backscattered reconstruction was also conducted through the same piezocomposite transducer element at this fundamental frequency. We have shown in this configuration that the focal mapping can be achieved in a transcranial configuration without the backscatter enhancement by microbubbles.

### D. Transcranial Focal Beam Mapping

The proposed dual transmission/receiving mode ultrasound phased array system is designed for use in clinical brain therapy applications. One major challenge in such applications is to reconstruct the focal map via backscattered emission from brain tissue with collected transcranially RF data, with backscattered emissions encountering considerable transcranial pressure loss (~60% pressure loss at 500 kHz for one-time transmissions). We have demonstrated that using the microbubbles-equipped tube phantom as the strong reflector; the backscattered PSF can be successfully reconstructed transcranially, after performing phase aberration correction through a short-cycle pulse (see Fig. 7). Nevertheless, with the tissue-mimicking graphite phantom, we have shown that the coherent beamforming approach can successfully reconstruct the focal beam pattern while increasing the transmission pulse-length to achieve sufficiently high MSR levels because of the significant reduction of backscattering signal levels. Instead, for further transcranial focal beam mapping, we showed that the transmission pulse cycle to 20 can effectively improve the focal detection capability with reasonable axial resolution (see Fig. 9). A compromise exists and should thus be carefully

selected to consider both the axial resolution of the reconstructed focal beam as well as transcranial detectability.

### E. Implication of BBB Opening Procedure Guidance

Previous passive imaging approaches have been shown to detect and map cavitation activity through noncoherent [45], [47] or coherent beamforming approaches [40]. In coherent detection, cavitation activity mapping has also been attempted to correlate the estimated pressure with occurrence of BBB opening. However, previous passive imaging approaches use microbubbles to amplify the backscattering intensity, raising concerns for concurrently inducing CNS tissue or vascular damage [33], [40], [49]. This study proposes an alternative, which reconstructs the focal beam solely through tissue backscattering, thus avoiding CNS tissue bio-effects or vascular effects which might potentially result from short-burst low exposure levels with microbubbles. Although this proposed dual-mode configuration may not optimize the cavitation observation directly through the most relevant index including subharmonics, ultraharmonics, or second harmonics because of the narrow transducer bandwidth, we demonstrated that this configuration has a unique advantage for the transcranially reconstruction of the focal mapping without microbubbles, and the backscattered magnitude of reconstruction can linearly correlate with the exposure level [see Fig. 10(c)]. This implies that preoperative focal beam mapping reconstruction could potentially not only perform focal mapping, but also power-adjustment for treatment exposure. Although the present study only demonstrates the feasibility of BBB opening applications, other applications such as CNS thermal ablation and CNS neuromodulation via focused ultrasound also require preoperative control and estimation of the transcranial exposure levels and could potentially be applied in these applications.

### F. Limitation of the Dual-Mode Setup

In this study, the phase correction procedure is only verified with a prior *ex vivo* calibration condition. Phase correction implementation relied on either the sound source being located at the geometry center to generate RF pulse for individual channel receiving for phase correction, or to perform individual RF data receiving for individual channel and measure the time of arrival via hydrophone located at the geometrical center as an alternative [40], [42], [48], [55]. This study used the positioning of the point reflector to enhance backscattering acquisition for phase aberration estimation, which is not realistic in clinical applications. To correct transcranial phase aberrations can use computed tomography (CT)-based [56]–[59] or MR-based [60], [61] treatment planning for theoretical model transcranial wave propagation. *In vivo* transcranial phase aberration correction is yet to be confirmed, but must be further developed in this dual transmit/receive mode system incorporating CT-based treatment planning to realize transcranial focal mapping in clinical applications.

The dual-mode concept has recently also been proposed by Heymans *et al.* [62], Haller and Wilkens [63], and Haller *et al.* [64] using a single-element focused ultrasound

setup to observe microbubble-seeded (or microbubble-absent) cavitation effect. The former uses a separated oscilloscope to improve reception detection sensitivity, and the latter uses a directional coupler to obtain reflected power which is linearly correlated with the reflected acoustic wave. The major constraint of the dual-mode operation is the limited bandwidth of the air-backed FUS transducer to receive second harmonic or subharmonic/ultraharmonics that can correlate to stable or microbubble-seeded cavitation activity. In bubble-seeded *in vitro* conditions, Heymans *et al.* [62] reported correlations of cavitation level to the third harmonic or fifth harmonic of the FUS transducer frequency. This might provide a solution for using the dual-mode concept to monitor cavitation-related effects due to the employed piezocomposite transducer provides third harmonic piezoelectric conversion capability.

When considering the use of this configuration for stable cavitation mapping and characterization, an alternative to subharmonic and first ultraharmonic emissions detection (i.e., emissions at 250 or 750 kHz, respectively) could be accomplished by specifically conducting transducer matching at these frequencies. This serves as a future direction for developing systems capable of transmission/receiving with flexible frequency band selection.

## VI. CONCLUSION

This study demonstrates the feasibility of using a multi-channel transmission/receiving mode ultrasound phased array system to concurrently perform ultrasound exposure and focal map reconstruction. Through the coherent transmit/receive hardware structure, a short-cycle pulse was used to reconstruct high-resolution PSF dimension approaching the wavelength level. The proposed coherent reconstruction allowed transcranial focal reconstruction on a weak-scattered tissue-mimicking phantom condition. Animal experiments for *in vivo* BBB opening demonstrate effective intraoperative focal beam mapping for procedure guidance. The results of this study may provide a useful reference for the development of therapeutic applications based on the dual-mode ultrasound phased array.

## ACKNOWLEDGMENT

The authors would like to thank the Center for Advanced Molecular Imaging and Translation, Chang Gung Memorial Hospital, Taoyuan, Taiwan, for their facility support.

## REFERENCES

- [1] E. A. Stewart *et al.*, "Focused ultrasound treatment of uterine fibroid tumors: Safety and feasibility of a noninvasive thermoablative technique," *Amer. J. Obstetrics Gynecol.*, vol. 189, pp. 48–54, Jul. 2003.
- [2] R. Catane *et al.*, "MR-guided focused ultrasound surgery (MRgFUS) for the palliation of pain in patients with bone metastases—Preliminary clinical experience," *Ann. Oncol.*, vol. 18, no. 1, pp. 153–165, Jan. 2007.
- [3] W. J. Elias *et al.*, "A pilot study of focused ultrasound thalamotomy for essential tremor," *New England J. Med.*, vol. 369, pp. 640–648, Aug. 2013.
- [4] S. Crouzet *et al.*, "Whole-gland ablation of localized prostate cancer with high-intensity focused ultrasound: Oncologic outcomes and morbidity in 1002 patients," *Eur. Urol.*, vol. 65, pp. 907–914, May 2014.
- [5] F. Wu *et al.*, "Extracorporeal focused ultrasound surgery for treatment of human solid carcinomas: Early Chinese clinical experience," *Ultrasound Med. Biol.*, vol. 30, no. 2, pp. 245–260, Feb. 2004.

- [6] K. Hynynen *et al.*, "MR imaging-guided focused ultrasound surgery of fibroadenomas in the breast: A feasibility study," *Radiology*, vol. 219, pp. 176–185, Apr. 2001.
- [7] N. McDannold, N. Vykhodtseva, S. Raymond, F. A. Jolesz, and K. Hynynen, "MRI-guided targeted blood-brain barrier disruption with focused ultrasound: Histological findings in rabbits," *Ultrasound Med. Biol.*, vol. 31, pp. 1527–1537, Nov. 2005.
- [8] K. Hynynen, N. McDannold, N. A. Sheikov, F. A. Jolesz, and N. Vykhodtseva, "Local and reversible blood-brain barrier disruption by noninvasive focused ultrasound at frequencies suitable for trans-skull sonications," *Neuroimage*, vol. 24, pp. 12–20, Jan. 2005.
- [9] L. H. Treat, N. McDannold, N. Vykhodtseva, Y. Zhang, K. Tam, and K. Hynynen, "Targeted delivery of doxorubicin to the rat brain at therapeutic levels using MRI-guided focused ultrasound," *Int. J. Cancer*, vol. 121, pp. 901–907, Aug. 2007.
- [10] K. C. Wei *et al.*, "Focused ultrasound-induced blood-brain barrier opening to enhance temozolomide delivery for glioblastoma treatment: A preclinical study," *PLoS ONE*, vol. 8, no. 3, p. e58995, 2013.
- [11] H. L. Liu, C. Y. Huang, J. Y. Chen, H. Y. Wang, P. Y. Chen, and K. C. Wei, "Pharmacodynamic and therapeutic investigation of focused ultrasound-induced blood-brain barrier opening for enhanced temozolomide delivery in glioma treatment," *PLoS ONE*, vol. 9, p. e114311, Dec. 2014.
- [12] M. Kinoshita, N. McDannold, F. A. Jolesz, and K. Hynynen, "Noninvasive localized delivery of Herceptin to the mouse brain by MRI-guided focused ultrasound-induced blood-brain barrier disruption," *Proc. Nat. Acad. Sci. USA*, vol. 103, pp. 11719–11723, Aug. 2006.
- [13] H. L. Liu *et al.*, "Focused ultrasound enhances central nervous system delivery of bevacizumab for malignant glioma treatment," *Radiology*, vol. 281, pp. 99–108, Oct. 2016.
- [14] H. L. Liu *et al.*, "Magnetic resonance monitoring of focused ultrasound/magnetic nanoparticle targeting delivery of therapeutic agents to the brain," *Proc. Nat. Acad. Sci. USA*, vol. 107, pp. 15205–15210, Aug. 2010.
- [15] C.-H. Fan *et al.*, "SPIO-conjugated, doxorubicin-loaded microbubbles for concurrent MRI and focused-ultrasound enhanced brain-tumor drug delivery," *Biomaterials*, vol. 34, pp. 3706–3715, May 2013.
- [16] P.-H. Hsu *et al.*, "Noninvasive and targeted gene delivery into the brain using microbubble-facilitated focused ultrasound," *PLoS ONE*, vol. 8, no. 2, p. e57682, 2013.
- [17] C. Y. Lin *et al.*, "Non-invasive, neuron-specific gene therapy by focused ultrasound-induced blood-brain barrier opening in Parkinson's disease mouse model," *J. Control Release*, vol. 235, pp. 72–81, Aug. 2016.
- [18] W. M. Pardridge, "The blood-brain barrier and neurotherapeutics," *NeuroRx*, vol. 2, no. 1, pp. 1–161, Jan. 2005.
- [19] P. C. Chu, H. L. Liu, H. Y. Lai, C. Y. Lin, H. C. Tsai, and Y. C. Pei, "Neuromodulation accompanying focused ultrasound-induced blood-brain barrier opening," *Sci. Rep.*, vol. 5, p. 15477, Oct. 2015.
- [20] P. P. Ye, J. R. Brown, and K. B. Pauly, "Frequency dependence of ultrasound neurostimulation in the mouse brain," *Ultrasound Med. Biol.*, vol. 42, pp. 1512–1530, Jul. 2016.
- [21] T. Deffieux, Y. Younan, N. Wattiez, M. Tanter, P. Pouget, and J. F. Aubry, "Low-intensity focused ultrasound modulates monkey visuomotor behavior," *Current Biol.*, vol. 23, pp. 2430–2433, Dec. 2013.
- [22] W. Legon *et al.*, "Transcranial focused ultrasound modulates the activity of primary somatosensory cortex in humans," *Nat. Neurosci.*, vol. 17, pp. 322–329, Feb. 2014.
- [23] E. A. Kaye, J. Chen, and K. B. Pauly, "Rapid MR-ARFI method for focal spot localization during focused ultrasound therapy," *Magn. Reson. Med.*, vol. 65, pp. 738–743, Mar. 2011.
- [24] E. A. Kaye and K. B. Pauly, "Adapting MRI acoustic radiation force imaging for *in vivo* human brain focused ultrasound applications," *Magn. Reson. Med.*, vol. 69, pp. 724–733, Mar. 2013.
- [25] L. Marsac *et al.*, "MR-guided adaptive focusing of therapeutic ultrasound beams in the human head," *Med. Phys.*, vol. 39, no. 2, pp. 1141–1149, 2012.
- [26] R. Paquin *et al.*, "Keyhole acceleration for magnetic resonance acoustic radiation force imaging (MR ARFI)," *Magn. Reson. Imag.*, vol. 31, pp. 1695–1703, Dec. 2013.
- [27] M. Gyöngy and C.-C. Coussios, "Passive spatial mapping of inertial cavitation during HIFU exposure," *IEEE Trans. Biomed. Eng.*, vol. 57, no. 1, pp. 48–56, Jan. 2010.
- [28] K. J. Haworth, K. B. Bader, K. T. Rich, C. K. Holland, and T. D. Mast, "Quantitative frequency-domain passive cavitation imaging," *IEEE Trans. Ultrason., Ferroelectr., Freq. Control*, vol. 64, no. 1, pp. 177–191, Oct. 2016.
- [29] K. J. Haworth *et al.*, "Trans-stent B-mode ultrasound and passive cavitation imaging," *Ultrasound Med. Biol.*, vol. 42, no. 2, pp. 518–527, Feb. 2016.
- [30] C. D. Arvanitis, C. Crake, N. McDannold, and G. T. Clement, "Passive acoustic mapping with the angular spectrum method," *IEEE Trans. Med. Imag.*, vol. 36, no. 4, pp. 983–993, Apr. 2017.
- [31] A. Haritonova, D. Liu, and E. S. Ebbini, "*In vivo* application and localization of transcranial focused ultrasound using dual-mode ultrasound arrays," *IEEE Trans. Ultrason., Ferroelectr., Freq. Control*, vol. 62, no. 12, pp. 2031–2042, Dec. 2015.
- [32] C. R. Jensen, R. W. Ritchie, M. Gyöngy, J. R. Collin, T. Leslie, and C. C. Coussios, "Spatiotemporal monitoring of high-intensity focused ultrasound therapy with passive acoustic mapping," *Radiology*, vol. 262, no. 1, pp. 252–261, Jan. 2012.
- [33] C. D. Arvanitis, M. S. Livingstone, and N. McDannold, "Combined ultrasound and MR imaging to guide focused ultrasound therapies in the brain," *Phys. Med. Biol.*, vol. 58, pp. 4749–4761, Jul. 2013.
- [34] C. R. Jensen, R. O. Cleveland, and C. C. Coussios, "Real-time temperature estimation and monitoring of HIFU ablation through a combined modeling and passive acoustic mapping approach," *Phys. Med. Biol.*, vol. 58, pp. 5833–5850, Sep. 2013.
- [35] J. Gateau, J. F. Aubry, D. Chauvet, A. L. Boch, M. Fink, and M. Tanter, "*In vivo* bubble nucleation probability in sheep brain tissue," *Phys. Med. Biol.*, vol. 56, pp. 7001–7015, Nov. 2011.
- [36] S. J. Norton and M. Linzer, "Backprojection reconstruction of random source distributions," *J. Acoust. Soc. Amer.*, vol. 67, no. 4, pp. 1802–1808, 1987.
- [37] S. J. Norton and I. J. Won, "Time exposure acoustics," *IEEE Trans. Geosci. Remote Sens.*, vol. 38, no. 3, pp. 1337–1343, May 2000.
- [38] J. Xia, P. H. Tsui, and H. L. Liu, "Low-pressure burst-mode focused ultrasound wave reconstruction and mapping for blood-brain barrier opening: A preclinical examination," *Sci. Rep.*, vol. 6, p. 27939, Jun. 2016.
- [39] J. Gateau, J.-F. Aubry, M. Pernot, M. Fink, and M. Tanter, "Combined passive detection and ultrafast active imaging of cavitation events induced by short pulses of high-intensity ultrasound," *IEEE Trans. Ultrason., Ferroelectr., Freq. Control*, vol. 58, no. 3, pp. 517–532, Mar. 2011.
- [40] M. A. O'Reilly, R. M. Jones, and K. Hynynen, "Three-dimensional transcranial ultrasound imaging of microbubble clouds using a sparse hemispherical array," *IEEE Trans. Biomed. Eng.*, vol. 61, no. 4, pp. 1285–1294, Apr. 2014.
- [41] H. L. Liu *et al.*, "Design and experimental evaluation of a 256-channel dual-frequency ultrasound phased-array system for transcranial blood-brain barrier opening and brain drug delivery," *IEEE Trans. Biomed. Eng.*, vol. 61, no. 4, pp. 1350–1360, Apr. 2014.
- [42] J. White, G. T. Clement, and K. Hynynen, "Transcranial ultrasound focus reconstruction with phase and amplitude correction," *IEEE Trans. Ultrason., Ferroelectr., Freq. Control*, vol. 52, no. 9, pp. 1518–1522, Sep. 2005.
- [43] H.-L. Liu, S.-M. Huang, and M.-L. Li, "High frame rate ultrasound monitoring of high intensity focused ultrasound-induced temperature changes: A novel asynchronous approach," *Med. Phys.*, vol. 37, pp. 5921–5928, Nov. 2010.
- [44] C. H. Farny, R. G. Holt, and R. A. Roy, "Temporal and spatial detection of HIFU-induced inertial and hot-vapor cavitation with a diagnostic ultrasound system," *Ultrasound Med. Biol.*, vol. 35, pp. 603–615, Apr. 2009.
- [45] J. J. Choi, R. C. Carlisle, C. Coviello, L. Seymour, and C. C. Coussios, "Non-invasive and real-time passive acoustic mapping of ultrasound-mediated drug delivery," *Phys. Med. Biol.*, vol. 59, pp. 4861–4877, Sep. 2014.
- [46] K. J. Haworth *et al.*, "Passive imaging with pulsed ultrasound insonations," *J. Acoust. Soc. Amer.*, vol. 132, pp. 544–553, Jul. 2012.
- [47] C. D. Arvanitis and N. McDannold, "Integrated ultrasound and magnetic resonance imaging for simultaneous temperature and cavitation monitoring during focused ultrasound therapies," *Med. Phys.*, vol. 40, no. 11, p. 112901, Nov. 2013.
- [48] M. A. O'Reilly, S. Rahman, J. Song, B. Lucht, and K. Hynynen, "Design and construction of a passive receiver array for monitoring transcranial focused ultrasound therapy," in *Proc. IEEE Ultrason. Symp.*, Oct. 2010, pp. 890–892.
- [49] M. T. Burgess, I. Apostolakis, and E. E. Konofagou, "Power cavitation-guided blood-brain barrier opening with focused ultrasound and microbubbles," *Phys. Med. Biol.*, vol. 63, p. 065009, Mar. 2018.



- [50] H. L. Liu *et al.*, "Magnetic resonance imaging enhanced by superparamagnetic iron oxide particles: Usefulness for distinguishing between focused ultrasound-induced blood-brain barrier disruption and brain hemorrhage," *J. Magn. Reson. Imag.*, vol. 29, no. 1, pp. 31–38, Jan. 2009.
- [51] H. L. Liu *et al.*, "Hemorrhage detection during focused-ultrasound induced blood-brain-barrier opening by using susceptibility-weighted magnetic resonance imaging," *Ultrasound Med. Biol.*, vol. 34, pp. 598–606, Apr. 2008.
- [52] N. McDannold, N. Vykhodtseva, and K. Hynynen, "Targeted disruption of the blood-brain barrier with focused ultrasound: Association with cavitation activity," *Phys. Med. Biol.*, vol. 51, pp. 793–807, Feb. 2006.
- [53] E. S. Ebbini, H. Yao, and A. Shrestha, "Dual-mode ultrasound phased arrays for image-guided surgery," *Ultrason. Imag.*, vol. 28, no. 2, pp. 65–82, 2006.
- [54] A. J. Casper, D. Liu, J. R. Ballard, and E. S. Ebbini, "Real-time implementation of a dual-mode ultrasound array system: *In vivo* results," *IEEE Trans. Biomed. Eng.*, vol. 60, no. 10, pp. 2751–2759, Oct. 2013.
- [55] M. Pernot *et al.*, "In vivo transcranial brain surgery with an ultrasonic time reversal mirror," *J. Neurosurg.*, vol. 106, pp. 1061–1066, Jun. 2007.
- [56] J. Song, A. Pulkkinen, Y. Huang, and K. Hynynen, "Investigation of standing-wave formation in a human skull for a clinical prototype of a large-aperture, transcranial MR-guided focused ultrasound (MRgFUS) phased array: An experimental and simulation study," *IEEE Trans. Biomed. Eng.*, vol. 59, no. 2, pp. 435–444, Feb. 2012.
- [57] J.-F. Aubry, M. Tanter, M. Pernot, J.-L. Thomas, and M. Fink, "Experimental demonstration of noninvasive transskull adaptive focusing based on prior computed tomography scans," *J. Acoust. Soc. Amer.*, vol. 113, no. 1, pp. 84–93, Jan. 2003.
- [58] G. Clement and K. Hynynen, "A non-invasive method for focusing ultrasound through the human skull," *Phys. Med. Biol.*, vol. 47, no. 8, pp. 1219–1236, Apr. 2002.
- [59] L. Marsac *et al.*, "Ex vivo optimisation of a heterogeneous speed of sound model of the human skull for non-invasive transcranial focused ultrasound at 1 MHz," *Int. J. Hyperthermia*, vol. 33, no. 6, pp. 635–645, 2017.
- [60] M. Wintermark *et al.*, "T1-weighted MRI as a substitute to CT for refocusing planning in MR-guided focused ultrasound," *Phys. Med. Biol.*, vol. 59, pp. 3599–3614, Jul. 2014.
- [61] G. W. Miller, M. Eames, J. Snell, and J. F. Aubry, "Ultrasound echo-time MRI versus CT for skull aberration correction in MR-guided transcranial focused ultrasound: *In vitro* comparison on human calvaria," *Med. Phys.*, vol. 42, no. 5, pp. 2223–2233, 2015.
- [62] S. V. Heymans, C. F. Martindale, A. Suler, A. N. Pouliopoulos, R. J. Dickinson, and J. J. Choi, "Simultaneous ultrasound therapy and monitoring of microbubble-seeded acoustic cavitation using a single-element transducer," *IEEE Trans. Ultrason., Ferroelectr., Freq. Control*, vol. 64, no. 64, pp. 1234–1244, Aug. 2017.
- [63] J. Haller and V. Wilkens, "Determination of acoustic cavitation probabilities and thresholds using a single focusing transducer to induce and detect acoustic cavitation events: II. Systematic investigation in an agar material," *Ultrasound Med. Biol.*, vol. 44, pp. 397–415, Feb. 2018.
- [64] J. Haller, V. Wilkens, and A. Shaw, "Determination of acoustic cavitation probabilities and thresholds using a single focusing transducer to induce and detect acoustic Cavitation events: I. Method and terminology," *Ultrasound Med. Biol.*, vol. 44, pp. 377–396, Feb. 2018.



**Hao-Li Liu** (M'07) received the Ph.D. degree in electrical engineering from National Taiwan University, Taipei, Taiwan, in 2003.

From 2004 to 2005, he was a Research Fellow with the Department of Radiology, Brigham and Women's Hospital, Boston, MA, USA, and also with Harvard Medical School, Boston, MA, USA. He is currently a Professor with the Department of Electrical Engineering, Chang Gung University, Taoyuan, Taiwan, and an Adjunct Researcher with the Division of Medical Engineering Research, National Health Research Institutes, Miaoli, Taiwan. He is currently continuing research in ultrasound thermal therapy and its treatment planning/simulation, ultrasound-induced blood–brain barrier disruption for brain drug delivery, and ultrasound phased array design.

Dr. Liu is a member of the International Society of Therapeutic Ultrasound (ISTU). He was a recipient of the Frederic Lizzi Award from ISTU to acknowledge his significant research contributions to therapeutic ultrasound.

**Chih-Hung Tsai**, photograph and biography not available at the time of publication.

**Chen-Kai Jan**, photograph and biography not available at the time of publication.

**Hsin-Yu Chang**, photograph and biography not available at the time of publication.

**Sheng-Min Huang**, photograph and biography not available at the time of publication.

**Meng-Lin Li**, photograph and biography not available at the time of publication.

**Weibao Qiu**, photograph and biography not available at the time of publication.

**Hairong Zheng**, photograph and biography not available at the time of publication.